J Mater Sci (2012) 47:208–226
DOI 10.1007/s10853-011-5788-x

Characterization of nonwoven structures by spatial partitioning of local thickness and mass density

D. Steven Keller · David L. Branca · Ohkyung Kwon

Received: 17 January 2011 / Accepted: 11 July 2011 / Published online: 28 July 2011
© Springer Science+Business Media, LLC 2011

Abstract In this investigation the distributions of local mass, thickness, and density for various nonwoven materials were mapped and analyzed. Non-contacting twin laser profilometry was used to map 10 mm square regions to a resolution of 25 μm. The areal distribution of mass was obtained using β-transmission radiographic imaging. Samples were selected from three common categories: nonwoven hybrids, polymer extruded nonwovens, and wet laid nonwovens. Several samples had embossed regions where the structure was compressed by melt bonding to impart strength. Structural maps were partitioned using binary masks to isolate the embossed features from the stochastic background structure. The joint distributions of thickness versus areal density were plotted and used to characterize the separated regions. Based on the structural distributions obtained from mapped regions, the background structure of most of the samples provided similar results to those observed for other stochastic fibrous web materials, such as paper. The wet laid samples and one spun-bonded extruded polymer nonwoven appeared stochastic with good correlation between local thickness and local areal mass density. In contrast samples with induced features such as embossing, melt bonding, and calendering show that thickness became independent of mass as a result. Examination of the thickness distributions within embossed regions for different samples showed different responses to compression that appeared dependent on material density and thickness.

D. S. Keller (✉)
Department of Chemical and Paper Engineering,
Miami University, Oxford, OH, USA
e-mail: kellerds@muohio.edu

D. L. Branca · O. Kwon
Department of Paper and Bioprocess Engineering,
SUNY College of Environmental Science and Forestry,
Syracuse, NY, USA

Introduction

The manufacture of nonwoven materials involves the complex engineering of the fibrous structure to attain the performance characteristics for a specific application. Unlike woven textiles, nonwovens are formed by the stochastic deposition of fibers or filaments into a web producing a non-uniform distribution of mass within the principal plane. The result are so-called inherent features, such as flocs, light weight zones, streaks and pinholes, the nature of which depends on the raw materials and the methods used to form the fibrous web. Additional processing, such as creping, embossing and localized thermal or adhesive bonding, maybe used to induce structural features that enhance the material properties. For example, by strengthening regions in a specific geometric pattern, bulky webs can be strengthened while retaining the pore structure needed for absorbency. The features that fall within the meso-scale region of the hierarchical structure of the web [1], i.e., from fiber diameters to tens of centimeters, can significantly influence tensile strength, flexural stiffness, permeability, absorbency, and optical properties. Thus, by separating the contributions that inherent and induced features have on the local web density, the web properties can be modeled and improved.

The objective of this investigation was to map the structural properties including areal density (grammage), thickness, and calculated volumetric density, of a variety of nonwoven materials and apply a partitioning algorithm to distinguish between inherent and induced inhomogeneities. Specifically, non-contacting profilometry and transmission

radiographic imaging were used to obtain data arrays for regions of interest of about 10 mm square to a resolution of 0.1 mm. Examination of the density maps and analysis of the relationships between thickness and areal density of the samples were used to compare the uniformity of densification within features and the surrounding region.

Many grades of nonwovens have material properties similar to paper, for which the methods for mapping thickness and areal density have been well-established. Representative maps of the in-plane, areal distribution of mass, the so-called formation, are acquired using optical [2–5] or radiographic transmission methods. The latter typically use β-ray [6–8], electron beam [9, 10], or grenz soft X-ray [11, 12] radiation sources, since these beams provide high contrast of the polymeric fibrous mass, while beam scattering within the structure is negligible [13, 14]. The spatial nonuniformity of attenuation, determined by mass, is commonly recorded using X-ray film [15, 16], or storage phosphor screens [17] and is directly related to the mass between the source and the detector. Images are then converted to areal density maps using a suitable calibration curve. A detailed investigation of β-radiographic imaging using the storage phosphor system as applied to paper was performed by Keller and Pawlak [8].

Non-contacting topographical methods for mapping the thickness of thin materials, such as films, foils or fibrous webs, were developed separately by Izumi and Yoshida [18] and Sung et al. [19, 20]. These methods offer an advantage over thickness determination by the analysis of optical or scanning electron micrographs in that a relatively large spatial area can be mapped (>1 cm square) to a resolution of <50 μm. Also, the optical topographical method is non-intrusive and non-destructive enabling the correlation with areal density maps obtained from radiography. X-ray microtomography has been introduced as a method for studying the structure of fibrous systems, especially to determine the distribution of mass and the pore structure [21, 22]. These methods provide a robust representation of the internal distribution of mass in three dimensions, with resolutions that greatly exceeds the current requirements. The present interest is in the mesoscale region in dimensions from 100 μm to areas 100 mm square.

The method of Sung et al. [20] is used in this study and based on an instrument referred to as the twin laser profilometer (TLP), shown in Fig. 1. The instrument simultaneously maps the surface topography of the two external surfaces of the sample. The principles of surface sensing by the instrument are illustrated in the inset in Fig. 1. The specimen is held vertically between two laser range sensors mounted in opposition on high precision position stages. The sensors use beam triangulation to determine the relative distance between each sensor and the reflective

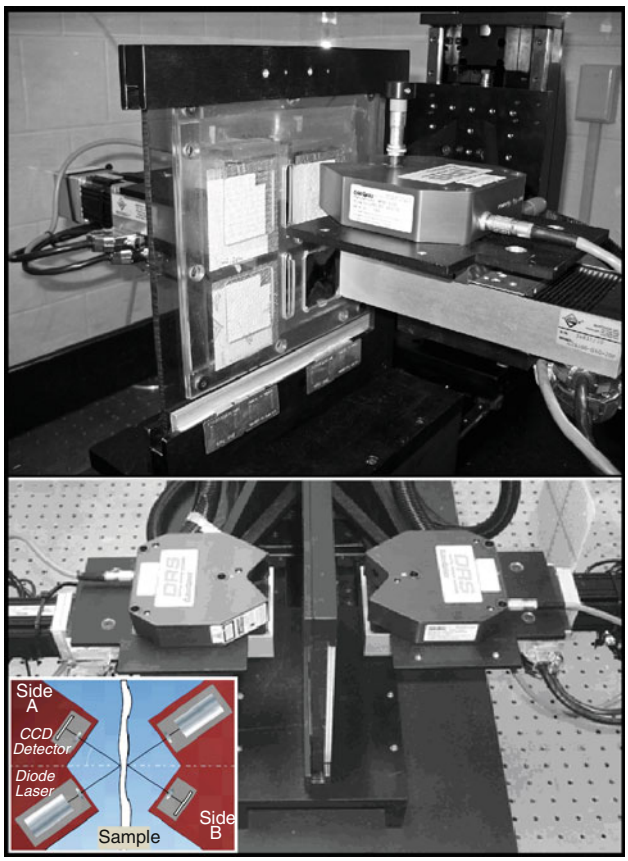

Fig. 1 Twin laser profilometer instrument (TLP)

surface, to a digital resolution of 0.35 μm and a repeatable precision of 1.0 μm over an operating range of 300 μm. Figure 1 shows the instrument where the positioning stages move the sensors along the z-axis, perpendicular to the principal (x–y) plane of the sample. In operation, the z-stages maintain the sensors to surface stand-off distance to within ~50 μm. Regions of interest in the x–y plane of the sample are mapped by translating the sensor/z-stage assemblies laterally (x) and vertically (y) to a selected sampling pattern with a minimum step of 1 μm. Thus, the TLP instrument can measure relative spatial position to a resolution of 1 μm in three dimensions, while mapping regions up to 100 mm square.

Sung et al. [19, 20] identified several potential artifacts that require consideration for reliable mapping of sample surfaces and subsequent calculation of local thickness. Surface detection depends on the ability of the incident beam to create a spot of diffuse or specular reflected light with a diameter of 10–20 μm. The shape and intensity of the spot detected by the sensor depends on roughness and continuity of the sample surface. For fibrous webs and porous solids with surface asperities finer than the beam spot size (~15 μm), the combined specular and diffuse reflectance is usually sufficient to accurately resolve the

surface. For highly reflective facets that are larger than the spot size and oriented at a large enough angles to the principal plane, the beam may be sufficiently diverted so that the surface is not detected. For surfaces that are discontinuous such that the incident beam penetrates the structure and is internally reflected, an accurate distance to the surface cannot be resolved. The materials examined in this study were selected to exhibit a low percentage these "dead spots". Sung et al. [19, 20] demonstrated that the occurrence of subsurface penetration of the beam resulting from either surface discontinuity, or fiber/bond transparency, may cause the measured thickness values to appear lower than actual. They demonstrated that by comparing an untreated region with one sputter coated to render fibers opaque, the extent of this artifact can be quantified.

The two opposing external surface maps acquired from the TLP instrument may then be used to calculate the local thickness and out-of-plane deformation at each position within the sampled region, as illustrated in Fig. 2, Branca et al. [23, 24] used the thickness and deformation maps to characterize the effects of embossing of tissue and towel papers. They found that in some cases the structure of the embossed features was crushed, while in others, the thickness was preserved and the feature was displaced out of the plane of the fibrous web.

By precisely aligning areal density and thickness maps, the local volumetric density can be determined at each point, and a density map may be generated for the entire region. Dodson et al. [25, 26] investigated the relationship between the distributions of mass, thickness, and density of paper samples by combining β-ray radiography with the thickness mapping method of Izumi and Yoshida [18]. They mapped laboratory made paper handsheets, composed of wood fibers with dimensions of about 2.2 mm $\times$ 37 μm, to a resolution of 1 mm within a 50-mm-square region. They observed a strong dependence of local thickness on the local areal density. They also found that a bivariate normal distribution could be used to model the relationship between local areal density and local thickness for near randomly dispersed and flocced fiber structures. The correlation between thickness and areal density maps was also observed by Sung et al. [20, 27] for sheets that were not subject to calendering. Induced densification by the calendering process was shown to disrupt the inherent relationship between local thickness and local areal density depending on the deformability of the compressing rolls. Calendering between chrome steel rolls preferentially densified thick, high grammage regions, thereby disrupting the correlation between thickness and grammage maps. However, soft-nip calendering between elastomeric

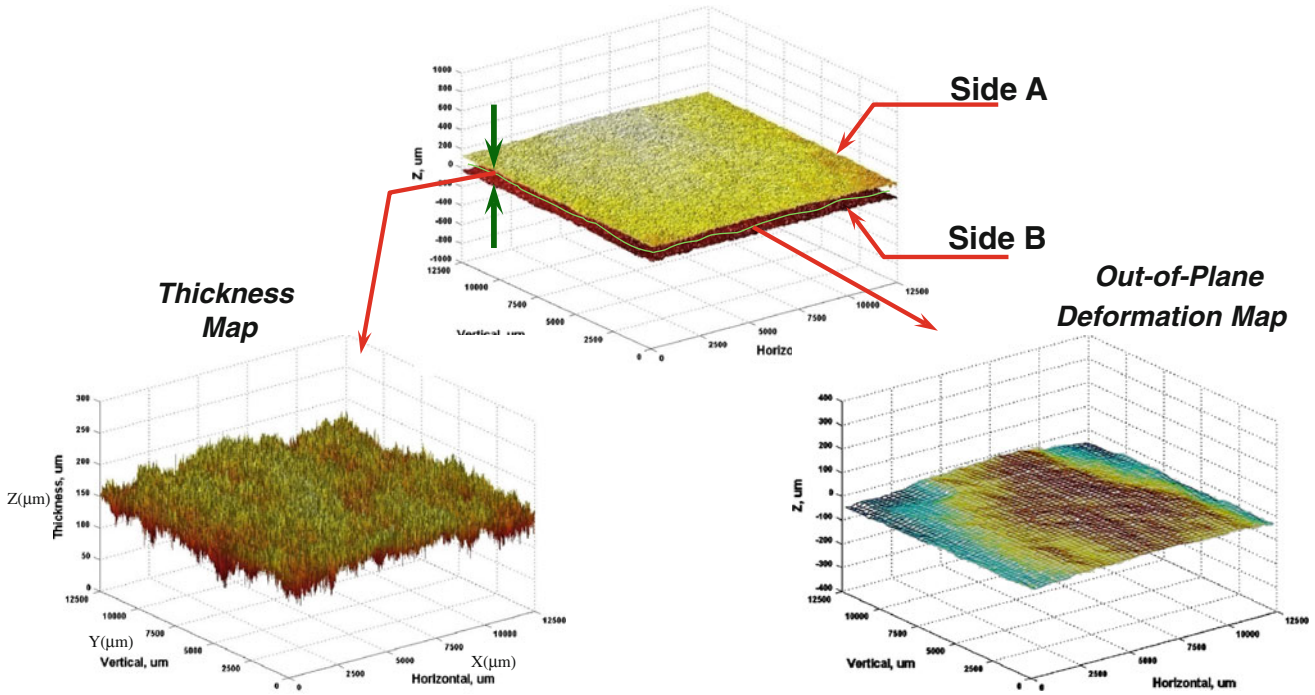

Fig. 2 An example of the data arrays obtained from the Twin laser profilometer (TLP) instrument. Opposing topographic maps are constructed by scanning a grid pattern and measuring the surface deflection at each position. The imaginary surface positioned halfway between the two surfaces represents the out-of-plane deformation of the scanned region. The difference between the two surfaces represents the local thickness map. Data set shown represents the maps for a 12-mm-square region of a newsprint paper [15]

surfaces compressed the web more uniformly so that a correlation between thickness and areal density remained, to some extent. It is with this consideration that this study explores the differences in structural densification with the embossed patterns of nonwovens as compared to the surrounding material.

Branca and co-workers [23, 24] characterized the induced features in tissues and towel papers formed by different processes. Thickness and areal density were mapped to a resolution of 100 μm in 10-mm square region. Features were isolated from the surrounding regions in the areal density, thickness, and density maps using masks based on the thresholding of out-of-plane deformation or thickness. By partitioning the structural maps, heterogeneities in the structure caused by stochastic distribution of fibers (inherent) were segregated from those induced through embossing or through drying. By partitioning structural maps of the nonwoven materials, the embossed and background regions on nonwovens will be sufficiently separated so that the change in structure can be quantified for analysis.

Experimental

Materials

The nonwoven samples were selected from the sample reference book supplied by INDA—Association of the Nonwoven Fabrics Industry [28]. The sample set included a variety of commercial products made by different forming processes including the wet-laid, polymer extruded, and hybrid processes. All samples had mean areal density less than 100 g/m^2. Low and high areal density samples were selected for each of the three forming types. The samples are identified in Table 1.

Table 1 Identification of the nonwoven samples

Sample	Formation/bonding	Fiber	Common use	Grammage (g/m^2)	Caliper (μm)
HY-1	Combination hybrid	(polymer)	Apparel liner	22.0	122
HY-2	Film/pulp laminate	(polymer)	Backsheet	35.0	189
PE-1	Meltblown entangle, cooled	Polypropylene	Filtration	20.0	149
PE-2	Flashspun—surface pattern	Polyethylene	Barrier	40.8	147
WL-1	Wet-laid, hot air	Wood pulp, vegetable	Tea bag	13.1	47
WL-2	Wet-laid, chemical	Wood pulp, synthetic	Wall covering	43.8	125

Measured gravimetric grammage and caliper thickness values are included

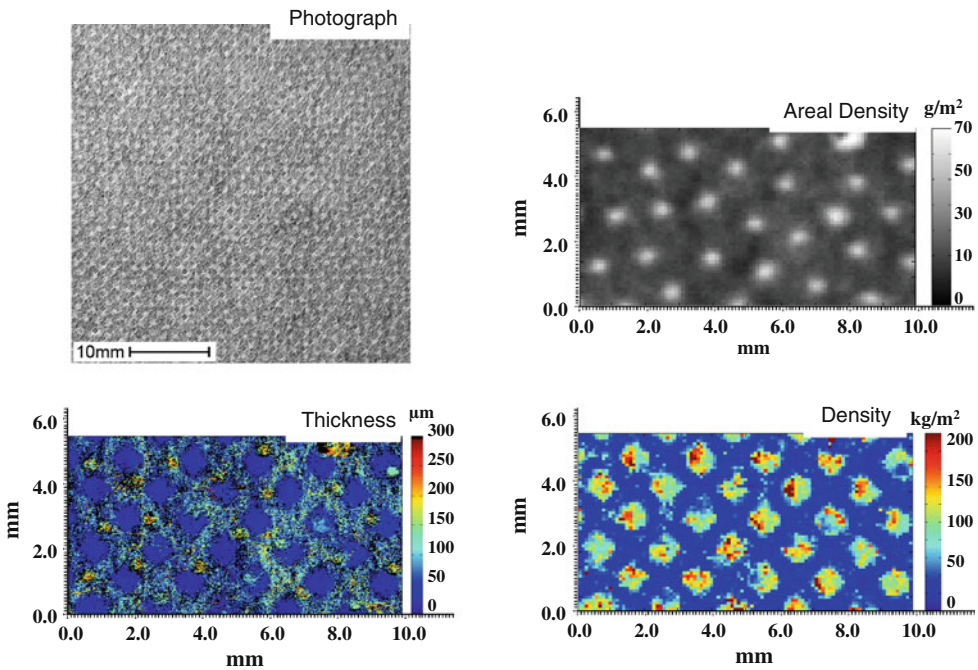

Fig. 3 Structural maps for sample HY-1. Light photograph of the 50 × 50 mm^2 sample (*top left*). Grammage (*upper right*) and density maps (*lower right*) of the scanned region, plotted at a resolution of 100 μm. Thickness map (*lower left*) plotted at a 25 μm resolution

Samples were trimmed to 70 × 70 mm^2 to fit the sample holder for the twin laser profilometer (TLP) instrument. The mean gravimetric grammage and flat platen caliper were determined using TAPPI Standard Method T410 [29] and T411 [30], respectively. Caliper values are expected to differ from the average thickness values determined from non-contacting methods. Caliper values will be lower for materials that are compressed under the pressure (50 kPa) applied by the steel platens. For materials that resist compression and have thickness non-uniformity at dimensions less than the platen diameter (16 mm), the caliper values may reflect an apparent thickness that is greater than that measured by integrating probe methods such as opposing spherical platens [31–33] or the TLP [20, 27]. The results for grammage and caliper are provided in Table 1.

The registration of areal density and thickness maps was facilitated by marking each sample with an optically and radiographically opaque foil. In order to test the extent of surface penetration that results from low surface scattering, small regions of the sample were sputter coated with gold–palladium to opacify the fiber surfaces. A Desk 2 (Denton Vacuum Co., Moorestown, NJ) cold sputter coater was used to deposit a uniform ~10 nm coating layer on the exposed surface. The details of this experimental of method for assessing the material transparency effects are given by Sung et al. [20]. Samples were conditioned under standard conditions according to TAPPI standard T-402 [34] prior to testing.

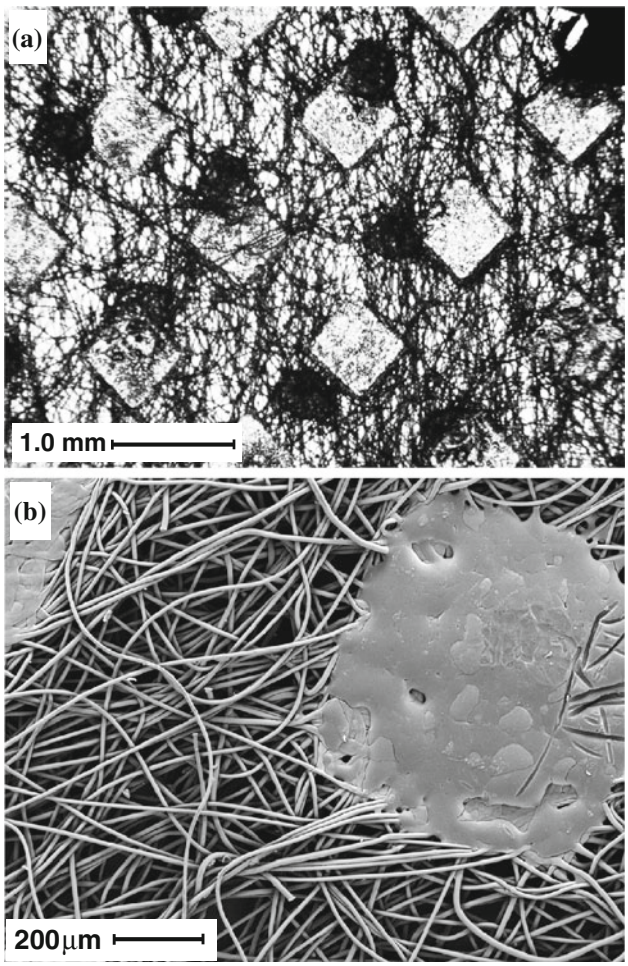

Fig. 4 Images of sample HY-1. Light transmission micrograph (**a**) and scanning electron micrograph (**b**)

Methods

Areal density mapping

The in-plane distribution of mass was mapped by β-radiographic imaging with a storage phosphor system by the procedure described in detail by Keller and Pawlak [8]. Samples were placed between a 200 × 200 mm^2 ^{14}C polymethyl methacrylate plate and storage phosphor screen for a 1 h exposure. Phosphor screens were then scanned using a PhosphorImager SI® (Molecular Dynamics, Sunnyvale, CA, USA) to digitize the latent image of the transmitted radiation into an array of discrete 100 μm square elements. Areal density values (g/m^2) for each element were calculated by using a Mylar step wedge and the procedure described by Keller and Pawlak [8]. For each sample, let (i, j) be the elements (pixels) in the ith row of the jth column in the areal density map, β, so that $\beta_{i,j}$ is the local areal density value. The mean areal density for the sampled region, $\bar{\beta}$, is defined by the relationship

$$\bar{\beta} = \sum_{i=1}^{N_x} \sum_{j=1}^{N_y} \frac{\beta_{i,j}}{N_x N_y} \quad (1)$$

where N indicates the total number of row, x, and columns, y, in the sample region.

Thickness mapping

Thickness maps were generated using the twin laser profilometer (TLP) instrument as described above. Samples were affixed to the sample frame at the top, and restrained from curl at the edges. A 10.0-mm-square region was selected for scanning such that the reference marker was recorded at the top edge. Surface positions of both sides were mapped and the local thickness values were calculated. The step interval in both the x and y directions was 25 (±1) μm. Four thickness values were averaged to determine a single value of thickness, $h_{i,j}$, for a 100 μm square region within the thickness map, h. The mean thickness for the sampled region, $\bar{h}$, is defined by the relationship

$$\bar{h} = \sum_{i=1}^{N_x}\sum_{j=1}^{N_y}\frac{h_{i,j}}{N_x N_y} \tag{2}$$

Density mapping

The density at each location was determined by dividing the local areal density by local thickness, $\rho_{i,j} = \beta_{i,j}/h_{i,j}$. Matlab was used to process and analyze data sets. Areal density and thickness maps were coarsely aligned using the foil markers. Using a normalized two-dimensional cross-correlation algorithm, the correlation coefficients were maximized for the final registration [24, 35]. The final alignments were visually inspected to confirm alignment of structural features. This method provides alignment of the areal density and thickness maps to ±100 μm (one pixel) in two dimensions. Thus, density maps, ρ, were determined for the sampled region, with a mean density, $\bar{\rho}$, defined as:

$$\bar{\rho} = \sum_{i=1}^{N_x}\sum_{j=1}^{N_y}\frac{\beta_{i,j}}{h_{i,j}N_x N_y} \tag{3}$$

Spatial partitioning

Embossed features were isolated from surrounding regions by use of partitioning masks based on methods developed by Branca and co-workers [23, 24]. For samples HY-1 and HY-2 a point near the center of each embossed region was selected. The embossed regions of the mask were then isolated using an algorithm that selects pixels based on thickness values that fall within a preset tolerance of the reference point. A tolerance of ±20 μm was used so that the mask region was generally confined to the irregular spatial dimensions of each embossed feature. The mask for sample PE-2 was generated by manually selecting regions showing z-directional deflection in one of the profile maps. To simplify, the embossed or indented features that exhibit lower thickness values are denoted by a subscript A. Surrounding "background" regions are identified with the subscript B. The thickness distribution of the entire sampled region, h, is comprised of subcomponents as:

$$h = \phi_A \sum_{i=1}^{N_x}\sum_{j=1}^{N_y}\frac{h_{A(i,j)}}{N_x N_y} + \phi_B \sum_{i=1}^{N_x}\sum_{j=1}^{N_y}\frac{h_{B(i,j)}}{N_x N_y} \tag{4}$$

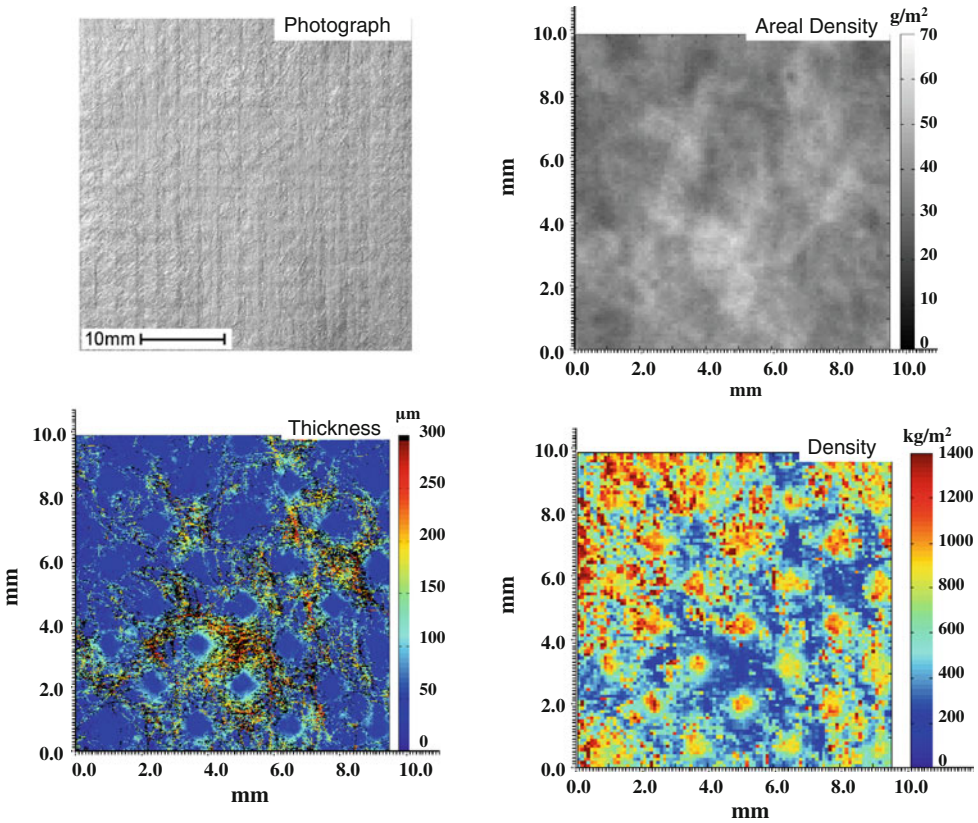

Fig. 5 Structural maps for sample HY-2. Light photograph of the 50 × 50 mm^2 sample (*top left*). Grammage (*upper right*) and density maps (*lower right*) of the scanned region, plotted at a resolution of 100 μm. Thickness map (*lower left*) plotted at a 25 μm resolution

where ϕ_A is the fractional contribution of the embossed area, and ϕ_B, for the surrounding area, where $\phi_B = 1-\phi_A$.

Results and discussion

Nonwoven hybrids

Structural properties

The structural maps for the combination hybrid sample HY-1 are provided in Fig. 3. An incident light photograph is included to show the complexity of the texture created by fiber deposition and the induced structures. As this sample has a relatively low mean grammage of $\bar{\beta} = 22.0\,\mathrm{g/m^2}$, the dark backing support is visible through the pinholes present in the web. The sample has two induced patterns that are evident in the light transmission micrograph shown in Fig. 4a. The diamond shapes are formed by melt-bonding the polymer fibers to impart strength. The shapes appear brighter in transmission since scattering surfaces are reduced in the process. The SEM image in Fig. 4b shows the melted region. The thickness map shown in Fig. 3 enables one to compare the thinning that occurs in the melted regions with the surrounding web. Note that pixels that are black indicate that one or both of the surfaces was not detected. For low grammage samples this is likely a pinhole where a void in the web exists. Examination of the areal density map indicates no detectible in-plane migration of mass occurred during the fusing process. However, a secondary pattern of high areal density regions is visible in the areal density map. These spots also appear to have higher thickness values than the background regions. These features result from the addition of an adhesive used when this nonwoven is bonded to fabrics when prepared for use as a fusible interlining. Further evidence of the adhesive may be seen in Fig. 4a. The density maps quantify the densification that occurs in both the melting process as well as filling the structure with adhesive.

A higher weight film/pulp laminate hybrid, HY-2, is shown in Fig. 5. This sample has twice the grammage as HY-1. The stochastic distribution of fibers is evident on the surface of the sample in the light photograph. By comparing the areal density map with the thickness map, there is an apparent correlation between features, such as the irregularly shaped region of high areal density and thickness centered at $x = 5$ mm, $y = 3$ mm in Fig. 5. The relationship between local thickness and local areal density will be addressed in the next section.

Two induced structures are also evident in the light photograph image of the HY-2 sample. The first is a regularly spaced, vertically oriented, streak pattern with a wavelength of about 2.5 mm. The pattern does not appear in the thickness or areal density maps, but was observed in the out-of-plane deformation map (not shown). This suggests that the process that imparted this pattern neither compressed the structure nor displaced mass within the *x*–*y* plane to create the pattern. The second induced pattern is composed of fused diamond shapes, similar to that seen in the HY-1 sample. These features are indentations and do not appear to displace mass within the *x*–*y* plane based on the areal density map in Fig. 5. The density map shows considerable variation in density resulting from the

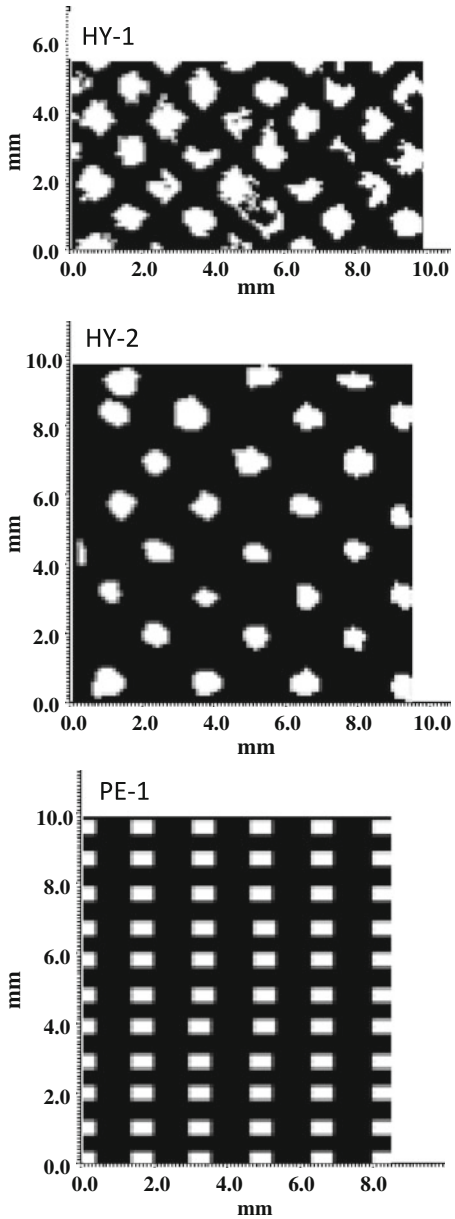

Fig. 6 Binary masks used to partition embossed features from the background region of the sample. The masks for HY-1 and HY-2 were generated using a threshold-flood fill algorithm. The mask for PE-2 was created by manually selecting rectangular regions containing the embossed features

forming process, as well as densification resulting from the fuse-bonding pattern. Additional insight for samples HY-1 and HY-2 is gained by examining the structural properties when the induced features are isolated by partitioning.

Structural partitioning

The structural properties for the melt-bonded regions for both the HY-1 and HY-2 samples were partitioned from the surrounding region using the selection process discussed in the Methods section. The binary masks created for partitioning are shown in Fig. 6. Note that the partitioning algorithm generates an irregularity of the shape of the embossed features that is specific to the region being sampled. The distributions of areal density and thickness are represented as histograms for samples HY-1 and HY-2 in Figs. 7 and 8, respectively. The shape of the areal density distributions for both samples is characteristic of other stochastic fibrous webs, and has been studied and modeled extensively [36, 37]. For both samples, the embossing process appears to have no effect on the distribution, suggesting that material was not significantly displaced within the principal plane during the embossing process. The radiographic mean and standard deviation values, provided in Table 2, quantify this observation, as the change in mean was less than 5% for the HY-1 sample, and less than 2% for the HY-2 sample.

With regard to thickness, the nature of the embossing was significantly different for the two samples. HY-1 had a bimodal distribution of thickness for the total sample, cf. Fig. 7. Upon partitioning, the distribution divided into two distinct distributions that had positive skewness. Thickness values and standard deviation are provided in Table 2. Mean thickness was reduced from 83 to 23 μm. The embossed and background distributions had less than 10% overlap, suggesting a sharp boundary between the two

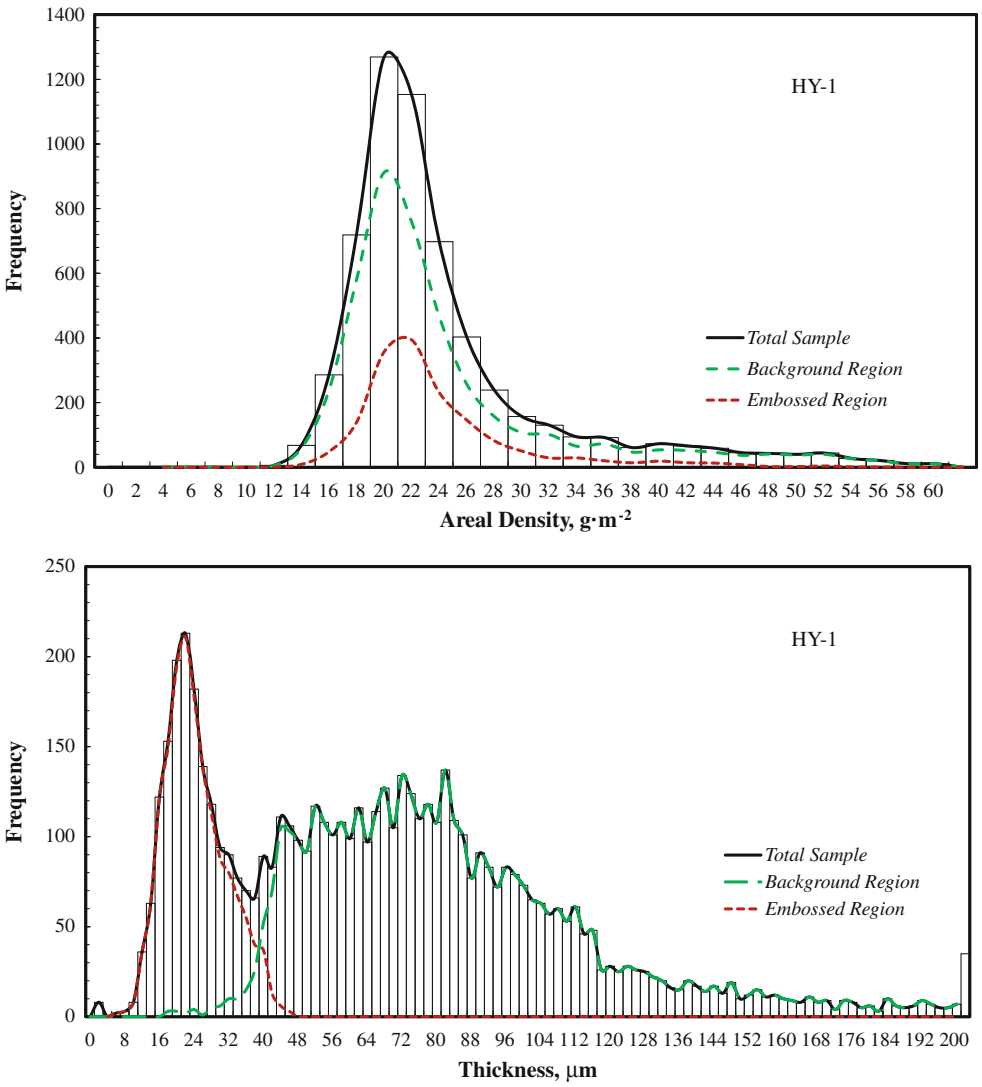

Fig. 7 Histogram plots of the areal density (*top*) and thickness (*bottom*) for the HY-1 sample. Graphs include the total sample distribution acquired from the entire test region in both line and bar form. The Back-ground and Embossed Regions determined from partitioning were used to generate respective histograms shown in *line* form (*dashed*)

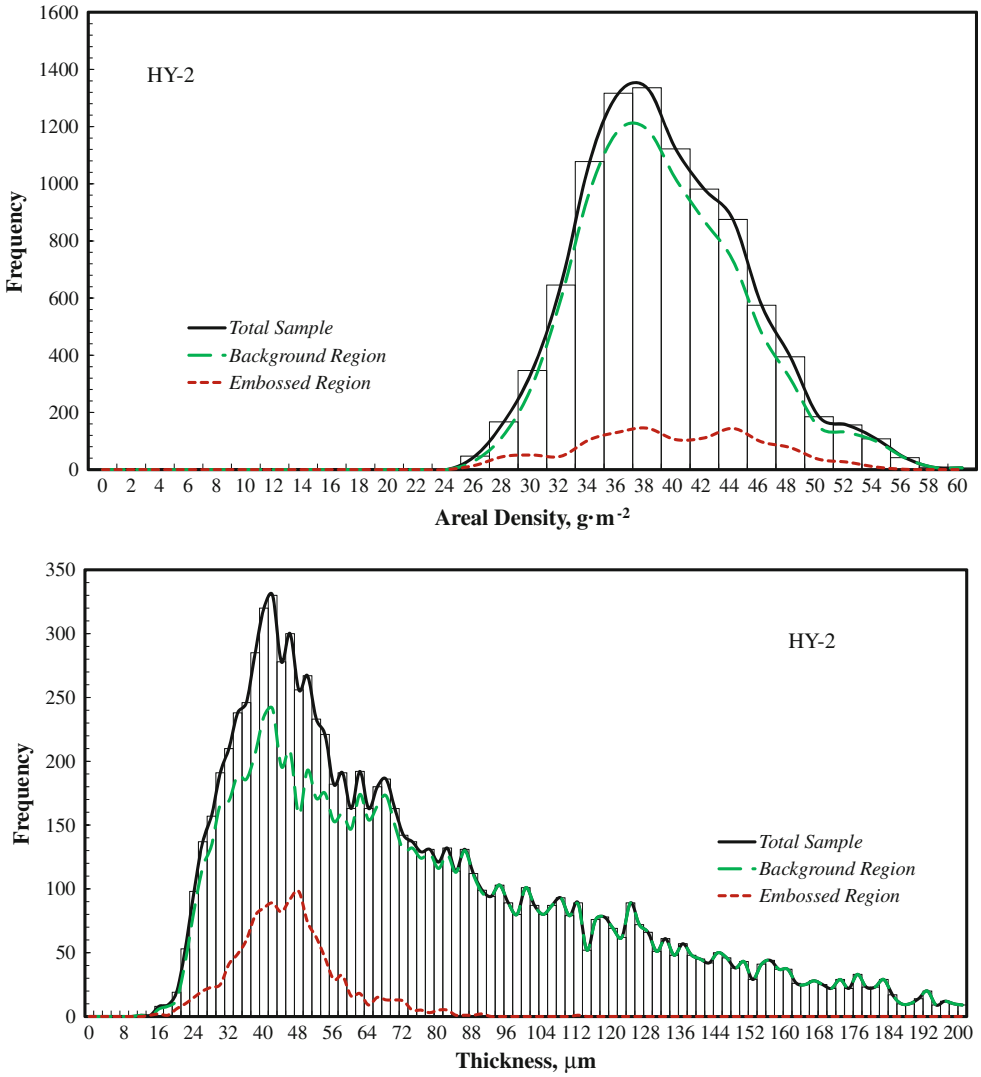

Fig. 8 Histogram plots of the areal density (*top*) and thickness (*bottom*) for the HY-2 sample. Graphs include the total sample distribution acquired from the entire test region in both line and bar form. The Background and Embossed Regions determined from partitioning were used to generate respective histograms shown in *line* form (*dashed*)

Table 2 Measured mean areal density and mean thickness values for nonwoven samples

Sample	Areal density (g m^{-2})		Thickness (μm)	
	Gravimetric	Radiographic mean (stdv)	Caliper	Profilometry mean (stdv)
HY-1	22.0		122	
(background)		23.8 (9.2)		83 (36)
(embossed)		22.7 (5.4)		23 (7)
HY-2	35.0		189	
(background)		38.2 (5.8)		82 (47)
(embossed)		38.8 (6.2)		44 (12)
PE-1	20.0	22.0 (5.5)	149	175 (38)
PE-2	40.8		147	
(background)		42.0 (7.5)		115 (24)
(embossed)		40.3 (7.5)		68 (20)
WL-1	13.1	9.8 (2.2)	47	18 (6)
WL-2	43.8	39.3 (4.2)	125	74 (18)

Standard deviations of distribution are shown in *parentheses*

regions. In contrast, the HY-2 sample had a highly skewed, unimodal distribution, cf. Fig. 8. When partitioned, the distribution of thickness within the embossed region, centered at a mean value of 44 μm, cf. Table 2, also constituted a substantial portion of the surrounding region. The breadth of the distribution, indicated by the standard deviations, and coefficients of variation (HY-1: 43% and HY-2: 57%) indicates that the nonuniformity of thickness, in both background structures, is quite high.

The relationship between thickness and density was examined further by plotting the joint probability distribution for the embossed and background data. Figure 9 illustrates the plots for HY-1 (top) and HY-2 (bottom) where thickness is plotted as a function of areal density. For each distribution, a single contour isoline of the cumulative probability density that encompasses 95% of the data points is included to assist in visualization of dominant shape of the distributions. For HY-2, the inset shows a plot of the background distribution with all data points plotted within the isoline line. The mean value of the thickness and areal density, given in Table 2, are marked by a symbol, a square for the background and a circle for the embossed regions. The distributions were analyzed using a scale invariant, least products regression known as reduced major axis (RMA) or geometric mean function [38] to determine the correlation between the two variables. Regression lines are plotted on the graphs, and the coefficients with respective standard deviations (stdv) are provided in Table 3. The reciprocal of the slope of the regression line provides an aggregate density for the distribution. These density values tend to lower than the average local density values calculated from each data point, also provided in Table 3. The two densities approach each other for samples with distribution regression lines that pass close to the origin, such as HY-1 and PE-1, which will be discussed in detail below.

Significant differences exist between the HY-1 and HY-2 distributions shown in Fig. 9. For example, for a bivariate normal distribution, one would expect the line of regression to pass through the origin. For HY-1, the intercepts for both the background and embossed distributions are quite close, −9.5 and −4.6, respectively. However, both distributions are quite dispersed relatively low correlation coefficients of 0.272 and 0.033, respectively. In contrast, the distributions for the HY-2 sample had much higher correlation, 0.63 for both background and embossed distributions. Neither of the regression lines for HY-2 passed through the origin, indicating that these distributions are not well-represented by a normal distribution. Rather, the density distribution for both partitions is expected to have zones of relatively high density.

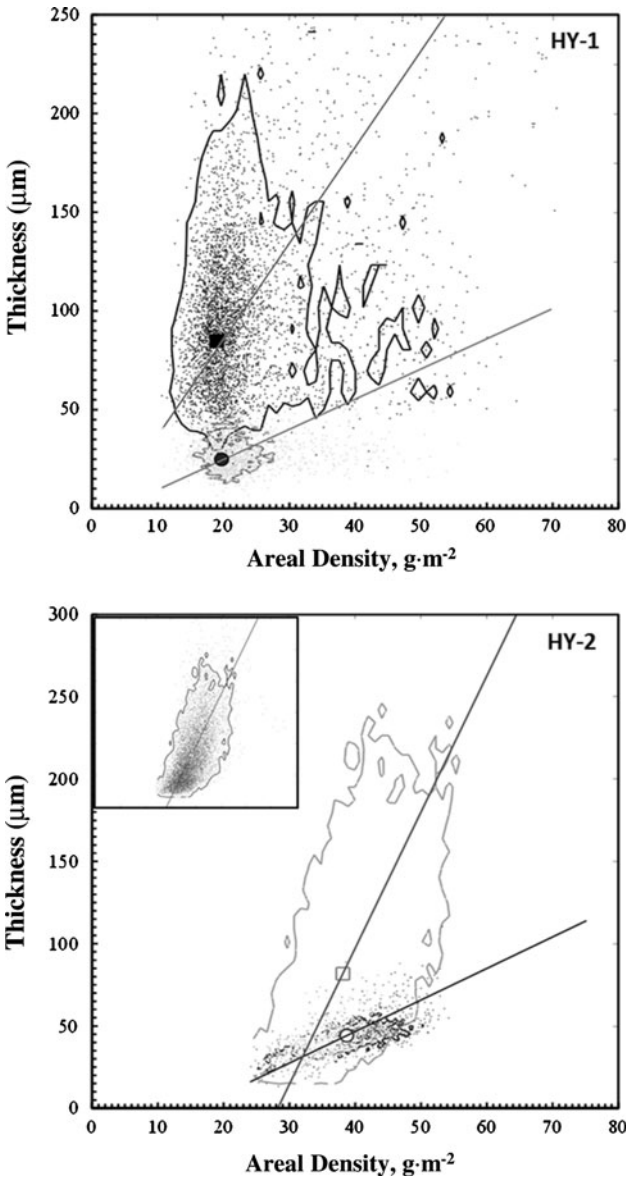

Fig. 9 Distribution of thickness versus grammage for samples HY-1 (*top*) and HY-2 (*bottom*). The background region extends to thicker values and is marked with a *square* at the mean of the distribution. The embossed region is marked with *circles* in the center. *Lines* indicate the RMA least product regressions of the distributions

The histogram plots of density for samples HY-1 and HY-2 are illustrated in Fig. 10. Density values were calculated using Eq. 3 at each location within the sampled area, with the mean density values given in Table 3. The distinct differences between the HY-1 and HY-2 background regions are apparent. The HY-2 distribution is broad with significant positive skewness. This indicates a large amount of densified area unassociated with the induced indentation pattern. Inspection of the density map for HY-2, cf. Fig. 5, showed larger regions of high and low density that coincided with the stochastic flocced structure

Table 3 Volumetric density data determined from areal density and thickness maps

Also the statistical coefficients derived from the RMA product regression of the joint distributions of thickness and areal density

Sample	Density (kg m^{-3})		Joint distribution		
	Mean (stdv)	COV	Slope (kg^{-1} m^3 10^3) (stdv)	Intercept (μm) (stdv)	Correlation coefficients
HY-1					
(background)	320 (157)	0.49	3.90 (0.07)	−9.5 (1.8)	0.272
(embossed)	1060 (323)	0.37	1.23 (0.04)	−4.6 (1.0)	0.033
HY-2					
(background)	597 (295)	0.49	8.27 (0.08)	−233 (3.0)	0.631
(embossed)	902 (181)	0.20	1.91 (0.05)	−30 (1.9)	0.630
PE-1	124 (24)	0.25	7.2 (0.06)	18.9 (1.4)	0.651
PE-2					
(background)	377 (77)	0.20	3.159 (0.03)	−17.8 (1.5)	0.579
(embossed)	631 (146)	0.23	2.66 (0.55)	−39.6 (2.3)	0.686
WL-1	591 (219)	0.37	2.95 (0.04)	−10.7 (0.5)	0.199
WL-2	559 (136)	0.24	7.167 (0.17)	18.9 (7.3)	0.651

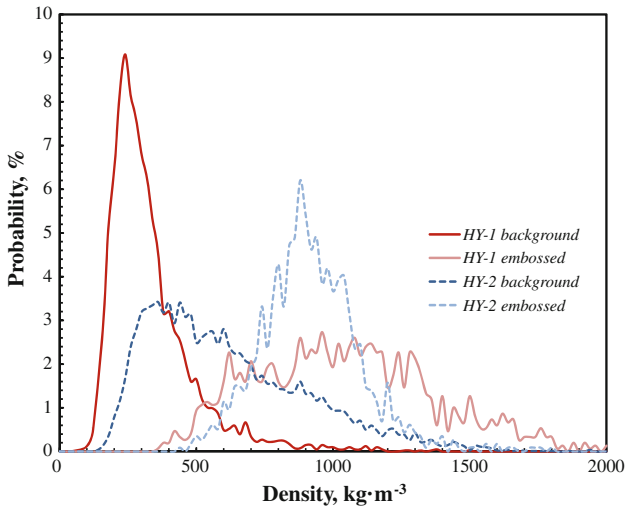

Fig. 10 Histogram plots (*line form*) of the volumetric density for the HY-2 (*solid*) and HY-2 (*dashed*) samples. For both samples, the *Background* region distributions have a lower density (*darker lines*)

of the web, also visible in the areal density and thickness maps. From Table 3, the average density for the background region was 597 kg m^{-3} with a standard deviation of 295 kg m^{-3}. The thickness map shows clearly the impression of the fuser roll used in the melt-bonding process that preferentially indented the thicker region forming the pattern of diamond indentations. This pattern is less apparent in the upper left corner where the sample has less mass and is thinner and denser. However, since bonding seems only to have occurred at the surface of the higher grammage web, the feature distribution indicates that there exists a dependency between thickness and areal density within the embossed regions. Sample HY-1 showed a similar relationship between the compressed and surrounding region. However, the embossing process was more intense, as the background material with a mode of the thickness distribution at ~80 μm, was compressed to one-third of this thickness, i.e., ~24 μm. As density approached the limiting value for the melted polymer, a lower limit of thickness of ~8 μm is reached. The mean density of the embossed region for sample HY-1 was 1060 kg m^{-3} with a standard deviation of 323 kg m^{-3}.

Polymer extruded nonwovens

Structural properties

Figure 11 shows the structural maps for the polypropylene extruded nonwoven sample PE-1. This figure includes a light photographic image of the samples, and the three structural maps representing areal density, thickness, and density. The PE-1 sample did not have an embossed pattern and so partitioning was not performed. The process used to form PE-1 involves the deposition of thin filaments of polymer randomly onto a surface where they fuse and cool. The stochastic nature of this web is apparent in the light photograph provided in Figure 11. The histogram plots for areal density and thickness are shown in Fig. 12. Both form symmetrical distribution that could be readily modeled by one of several statistical functions used to characterize paper [37]. The mean areal density was found to be 22 g m^{-2} (stdv 5.5 g m^{-2}) and the mean thickness was 175 μm (stdv 38 μm) in Fig. 11, the areal density map shows a stochastic floccy pattern which is similar to that which is observed for wood fiber papers. A matching pattern is evident in the thickness map where regions with greater thickness also appear to have more mass. A calculated volumetric density is relatively uniform as seen in Fig. 13, where the histogram plots of density for PE-1 are presented with four other samples. Sample PE-1 has a

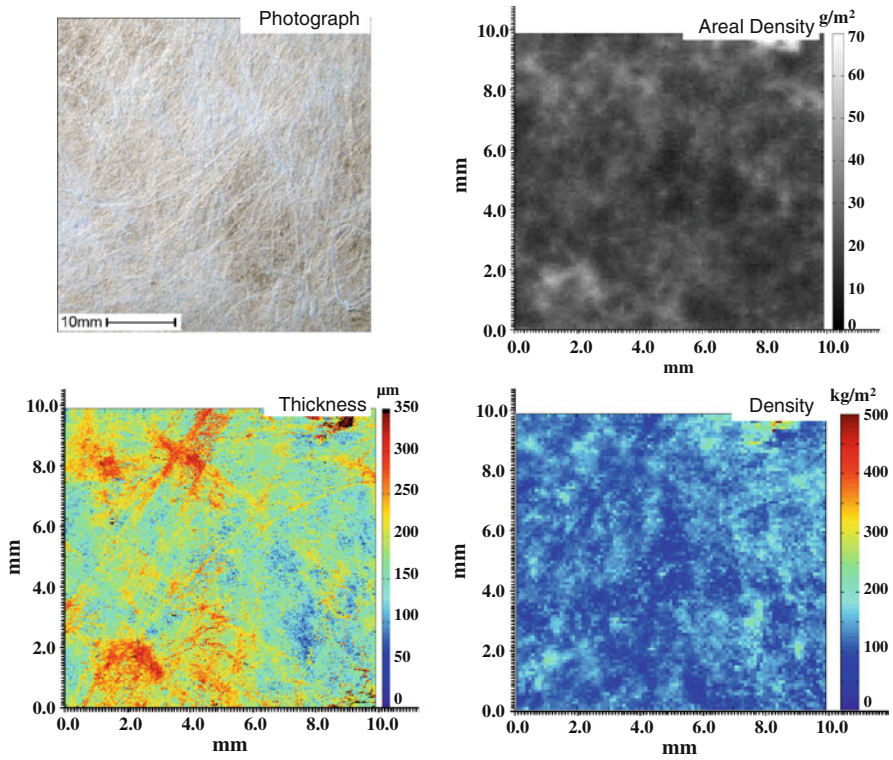

Fig. 11 Structural maps for sample PE-1. Light photograph of the 50 × 50 mm^2 sample (*top left*). Grammage (*upper right*) and density maps (*lower right*) of the scanned region, plotted at a resolution of 100 µm. Thickness map (*lower left*) plotted at a 25 µm resolution

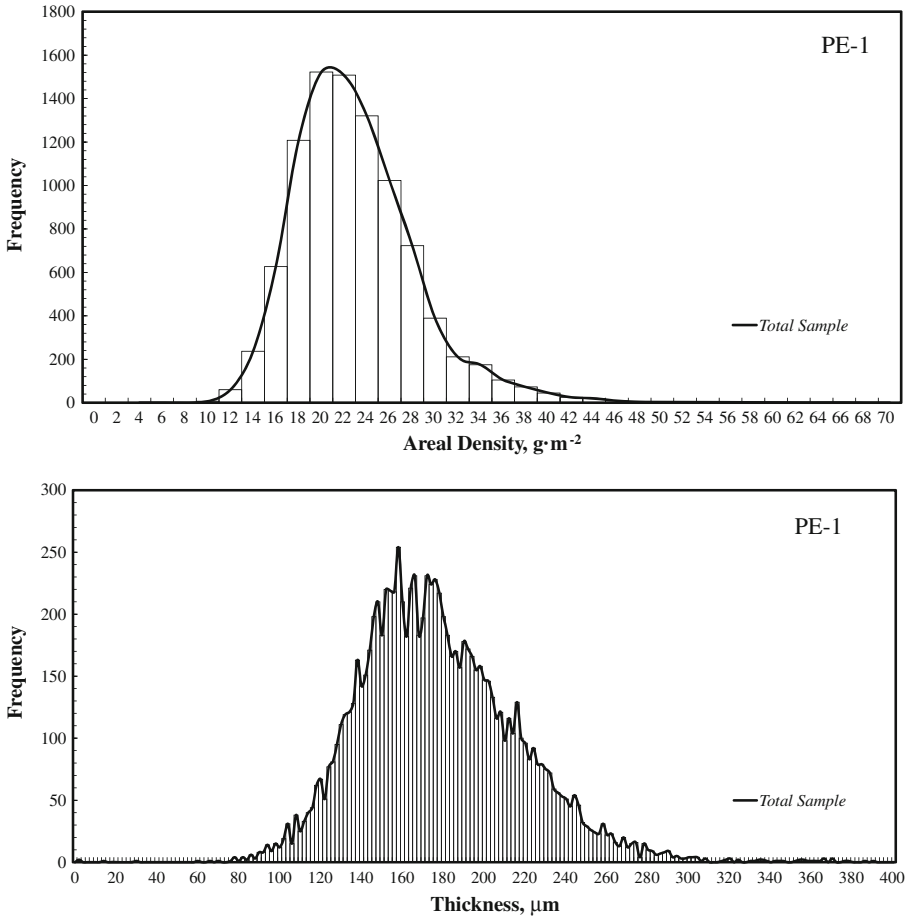

Fig. 12 Histogram plots of the areal density (*top*) and thickness (*bottom*) for the PE-1 sample. Graphs include the total sample distribution acquired from the entire test region in both *line* and *bar* form

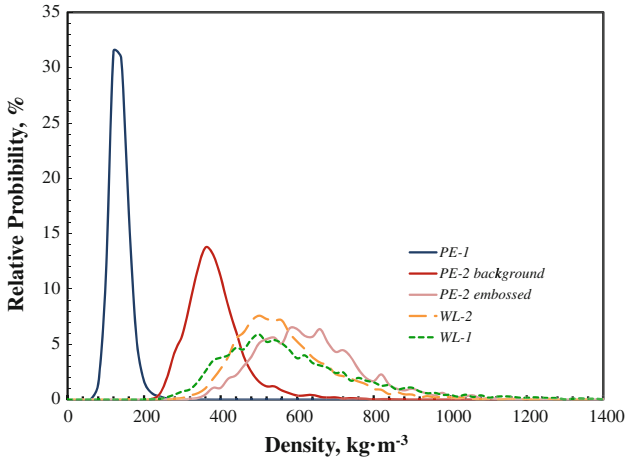

Fig. 13 Histogram plots (*line form*) of the volumetric density for the PE-1 and PE-2 (*solid*) and WL-1 and WL-2 (*dashed*) samples. For the PE-2 sample, the *Background* region distributions have a lower density (*darker lines*)

mean density of 124 kg m^{-3} (stdv 24 kg m^{-3}). The uniformity of this thick, low density web is characteristics of filtration materials.

The second polymer extruded sample, PE-2, was formed by the flash spinning of polyethylene fibers onto a surface to form a stochastic background structure. A regular pattern of indentations was then introduced into the structure as seen in the light photograph in Fig. 14. A second pattern of circular indentations is visible in the thickness map shown in Fig. 15. The areal density map in that same figure shows no indication of the embossed pattern, suggesting that the stochastic structure was compressed without a significant displacement of mass in the X–Y plane.

Figure 15 shows the areal density and thickness histograms for PE-2. The areal density distribution is also symmetrical. The mean areal density does not change significantly on densification as the structure is reduced from ~115 to ~68 μm in the embossed regions, see Table 2. Density nearly doubles from 377 to 631 kg m^{-3} in the process. The local thickness distribution shown in Fig. 15 is bimodal with the main peak centered at ~120 μm, and a shoulder centered at ~72 μm. Partitioning will be effective at isolating the characteristics of the embossed and background regions for further analysis.

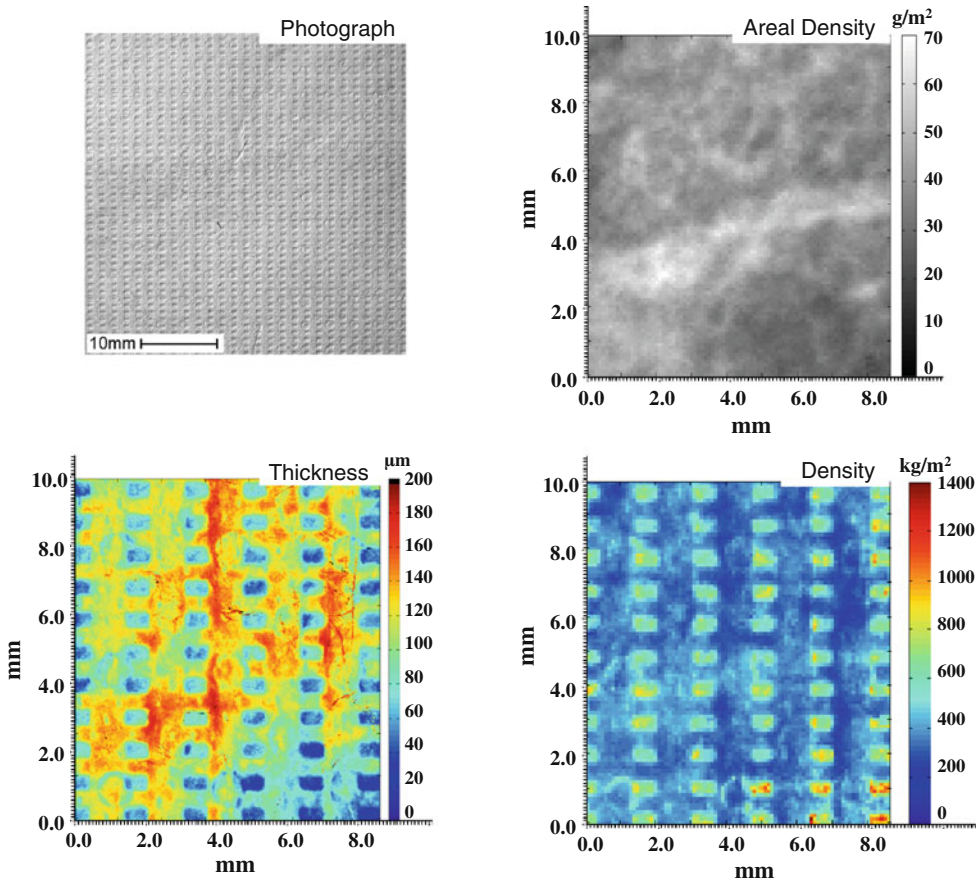

Fig. 14 Structural maps for sample PE-2. Light photograph of the 50 × 50 mm^2 sample (*top left*). Grammage (*upper right*) and density maps (*lower right*) of the scanned region, plotted at a resolution of 100 μm. Thickness map (*lower left*) plotted at a 25 μm resolution

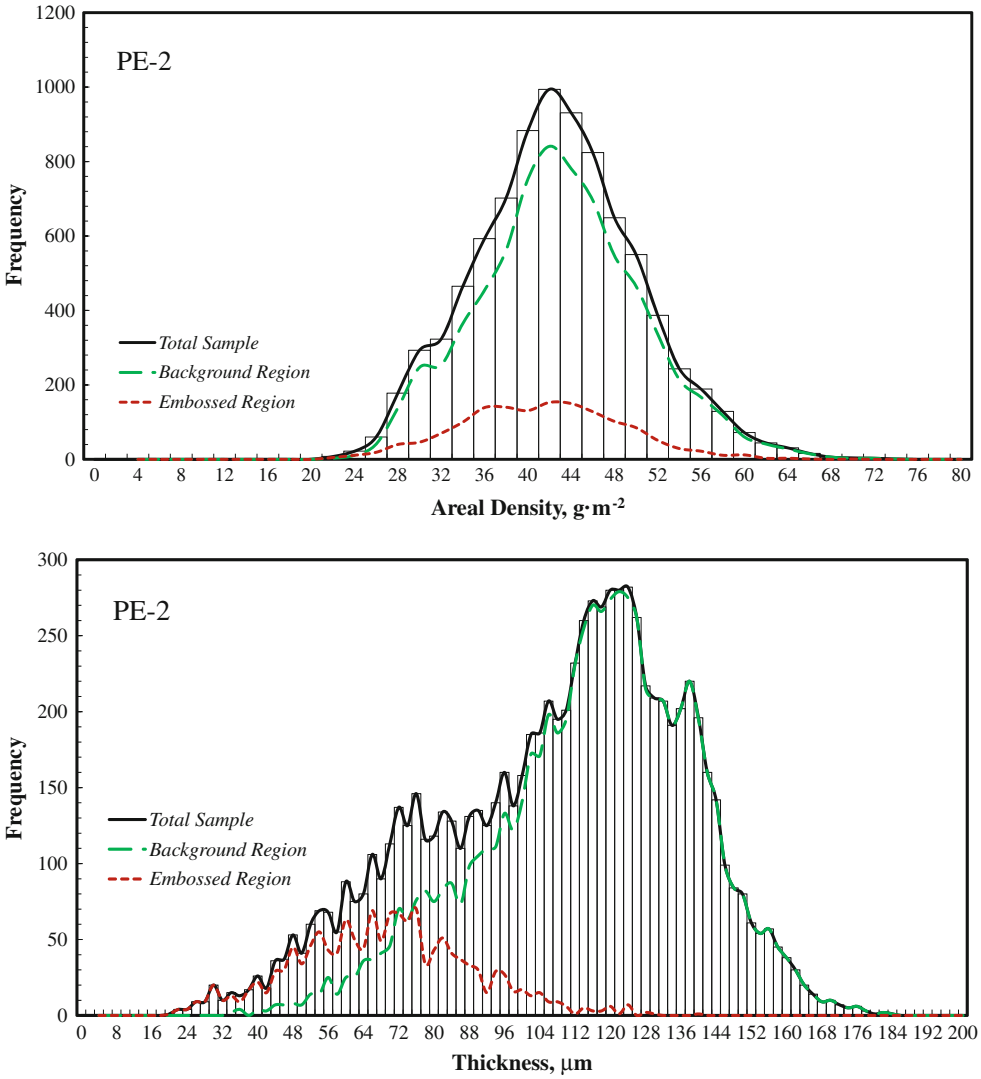

Fig. 15 Histogram plots of the areal density (*top*) and thickness (*bottom*) for the PE-2 sample. Graphs include the total sample distribution acquired from the entire test region in both *line* and *bar* form. The *background* and *embossed* regions determined from partitioning were used to generate respective histograms shown in *line* form (*dashed*)

Structural partitioning

The structural properties for the PE-2 sample were partitioned using a manually generated masked based on the rectangular dimensions of the indented features. Figure 6 illustrates the mask where the repetitive rectangular pattern is registered to the feature pattern of the sample, cf. Fig. 11. The separate maps of the indented features and the background region are not shown. In Fig. 12, the thickness histogram for the embossed region clearly accounts, in part, for the secondary shoulder. The mean thickness value for the embossed region was determined to be 68 µm (stdv 20 µm). The background thickness distribution had a negative skewness which may result in part from the circular indentations that were not included in partitioning.

The joint distributions of thickness versus areal density for samples PE-1 and PE-2 are provided in Fig. 16. For PE-2 the mean values of the distributions are marked by a square for the background and a circle for the embossed region. The RMA product regression line is plotted on the graphs. The correlation coefficients are 0.579 for the background and 0.686 for the embossed distributions.

The response of the PE-2 structure to embossing appears different than was observed for the HY-1 and HY-2 samples. When the hybrid samples were compressed, the thicker regions were deformed preferentially, thereby reducing the correlation between thickness and areal density. This response is quantified by the change of slope of the RMA regression line; cf. Fig. 9, from 3.90 to 1.23 for HY-1 and 8.27 to 1.91 for HY-2. In contrast, the slope of the RMA regression line for PE-2 changed much less, i.e., from 3.2 to 2.7, from Table 3. This suggests that a more elastic response of either the embossing die, or the PE-2 structure so that the thickness distribution translates uniformly to

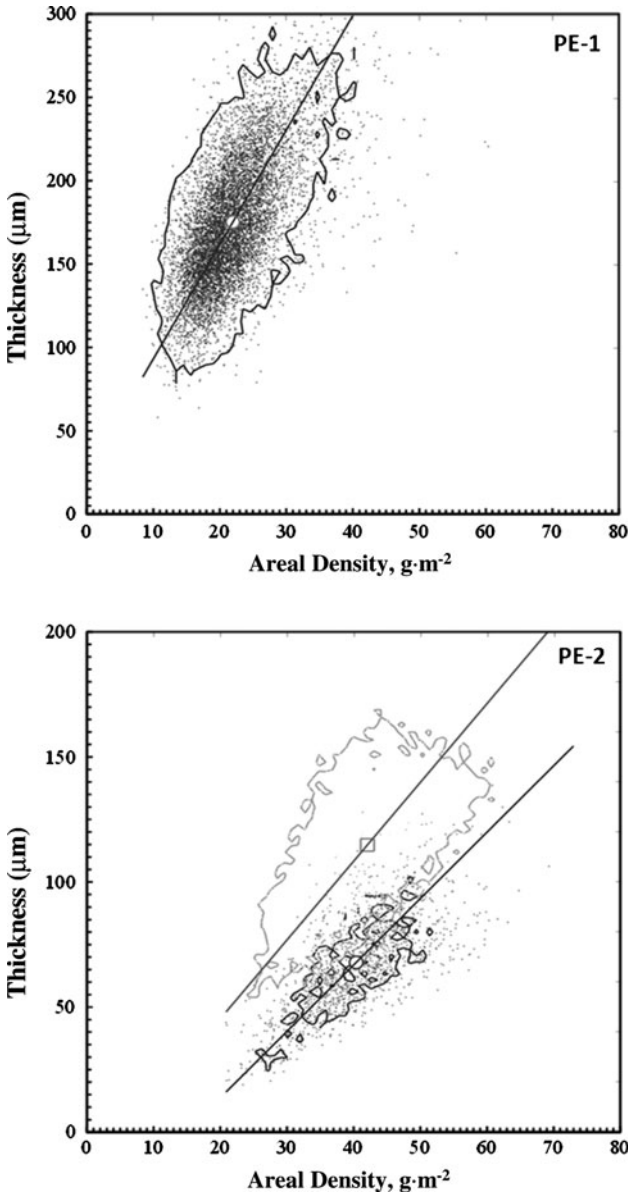

Fig. 16 Distribution of thickness versus grammage for samples PE-1 (*top*) and PE-2 (*bottom*). The *background region* extends to thicker values and is marked with a *square* at the mean of the distribution. The embossed region is marked with *circles* in the center. *Lines* indicate the RMA least product regressions of the distributions

lower thickness independent of original thickness or areal density. The PE-2 samples are 40% thicker than both HY samples, which may cause less plastic deformation during embossing. Figure 13 shows the density distributions for PE-2 background and embossed, which had coefficients of variation of 20 and 23%, respectively.

Figure 16 also shows the joint distribution of thickness and areal density for the PE-1 sample. The RMA regression line passes near the origin and the correlation coefficient was 0.651, which is consistent with the HY-2, PE-2, and WL-2 samples, cf. Table 3.

Wet laid nonwovens

Structural properties

Wet laid nonwovens have a structure that closely resembles that of communication papers. Fibers tend to be shorter and they are stochastically deposited from dilute suspension in the forming process. The photographs and maps of the structural properties are shown in Fig. 17 for sample WL-1 and Fig. 18 for sample WL-2. Both samples had a regular pattern with sub-millimeter spacing produced by the forming fabric or screen, which may be seen in the photographs. These features were also identified in the thickness maps, although the β-radiographic imaging had insufficient resolution to detect the pattern. For sample WL-1, the pinholes are evident in the photograph and also appear as black pixels in the thickness map where the surface was not detected and there appears to be a correlation between areal density and thickness for both samples.

Figure 19 shows the histograms for areal and density for the WL-1 and WL2 samples. Both samples have unimodal distributions that are near symmetrical about the mean values, which are provided in Table 2. The distributions for volumetric density of the two samples are plotted in Fig. 13 where the shapes are quite similar, as are the mean densities of 591 kg m^{-3} (COV = 0.37) for sample WL-1 and 559 kg m^{-3} (COV = 0.24)for sample WL-2.

The joint distributions of thickness and areal density for the two samples are plotted in Fig. 20. Sample WL-1 has a distribution that indicates that the two variables are relatively independent of one another as the correlation coefficient was 0.199. However, since this sample has very low grammage, and the radiographic imaging is unable to resolve individual fibers, the reliability of this method is lost for samples with areal density less than 10 g m^{-2}. At higher areal density, the WL-2 sample exhibited higher dependence of thickness on areal density. For this sample, the correlation coefficient was 0.651, which is consistent with several other samples tested in this study. In this case, the analysis is much less susceptible to errors resulting from low mass, such as pinholes, or the ability to resolve mass to a resolution below the measurement limits.

Conclusions

An overview investigation of six distinctively different nonwoven samples demonstrated the differences in the structural properties of areal mass density, thickness, and volumetric density, and the distributions thereof. A new approach for the characterization of the meso-scale structural properties of nonwoven materials was applied that

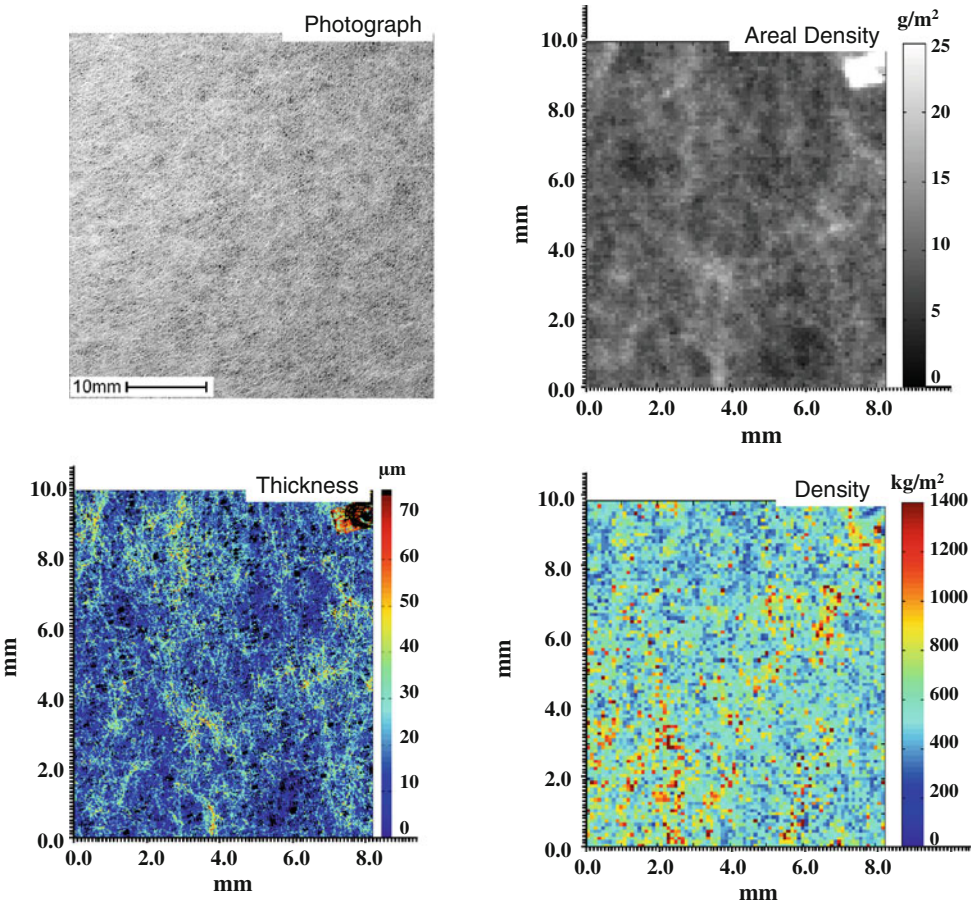

Fig. 17 Structural maps for sample WL-1. Light photograph of the 50 × 50 mm^2 sample (*top left*). Grammage (*upper right*) and density maps (*lower right*) of the scanned region, plotted at a resolution of 100 µm. Thickness map (*lower left*) plotted at a 25 µm resolution

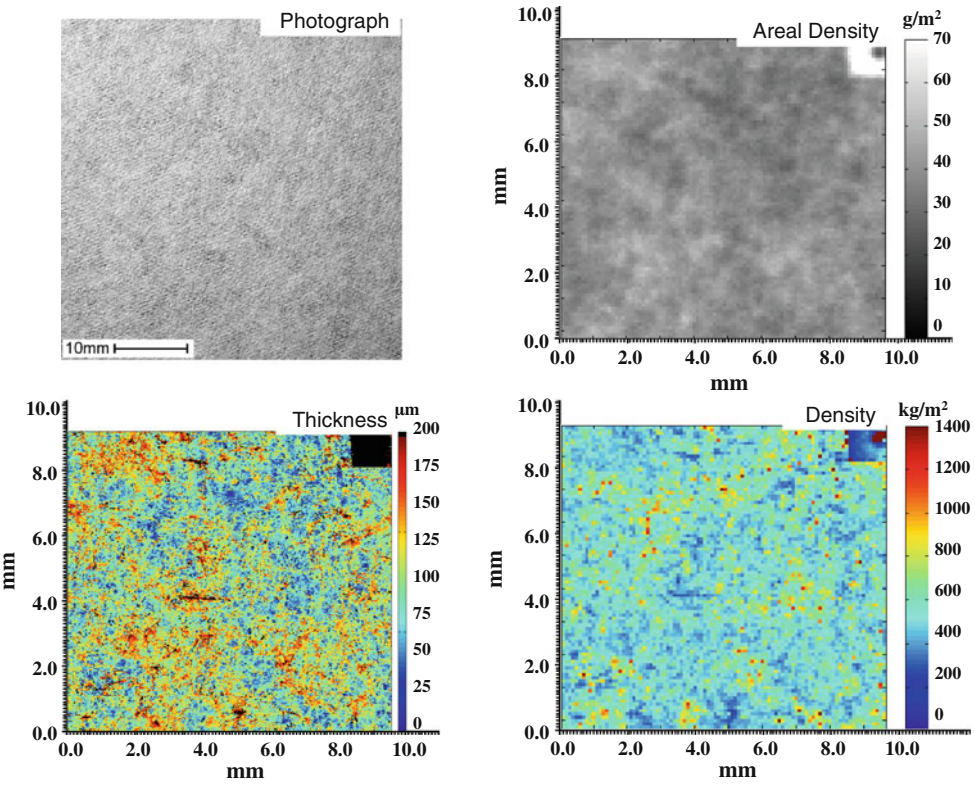

Fig. 18 Structural maps for sample WL-2. Light photograph of the 50 × 50 mm^2 sample (*top left*). Grammage (*upper right*) and density maps (*lower right*) of the scanned region, plotted at a resolution of 100 µm. Thickness map (*lower left*) plotted at a 25 µm resolution

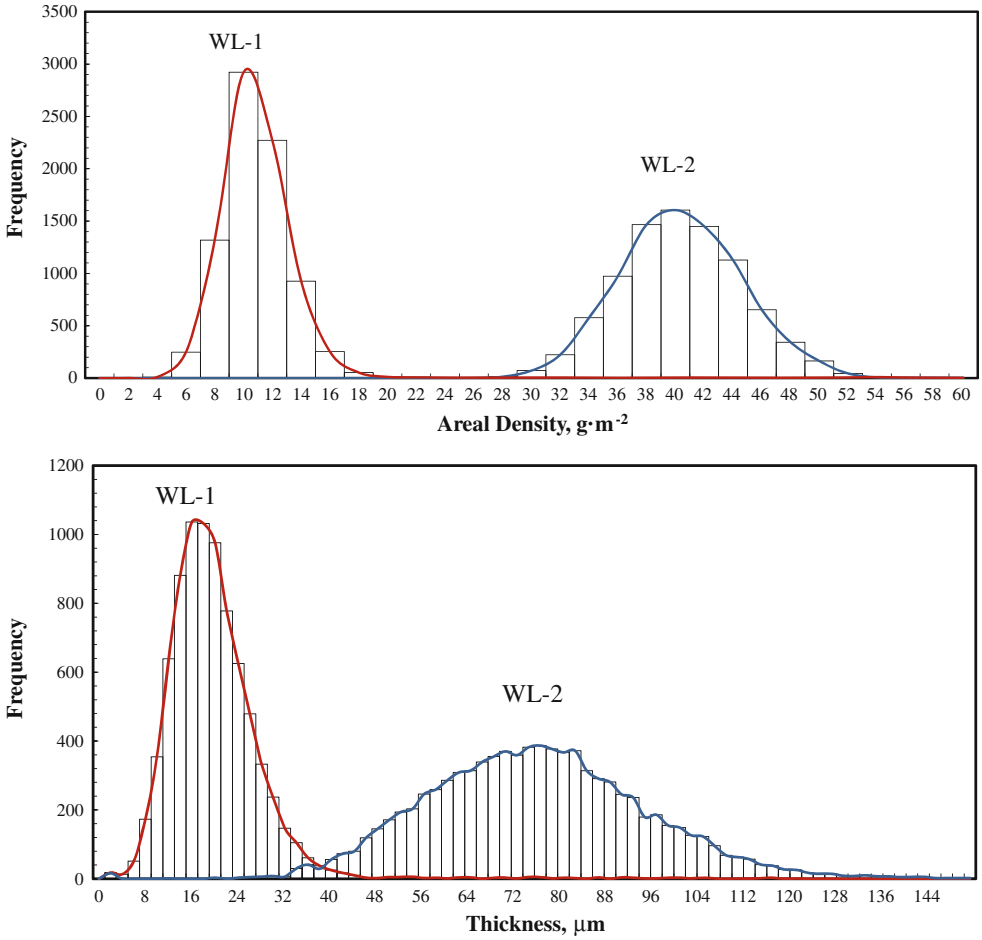

Fig. 19 Histogram plots of the areal density (*top*) and thickness (*bottom*) for the WL-1(*left*) and WL-2 (*right*) samples. Graphs include the total sample distribution acquired from the entire test region in both *line* and *bar* form

involved thickness mapping using non-contact laser profilometry and mapping of the in-plane distribution of mass using β-radiographic storage phosphor imaging. The local volumetric density was calculated from thickness and areal density maps to a resolution of 100 µm in 10 mm square regions. Several samples, including hybrid nonwovens and polymer extruded webs included embossed structures that contributed to the complexity of the materials. By partitioning structural maps, the mass, thickness and density distributions for the embossed region and the background region were separated and shown to quantify the effectiveness of the embossing process on structural changes.

For the two hybrid nonwovens, the thickness reduction at melt bonding sites was shown to be greater for one sample, HY-1: 72%, compared to the other HY-2: 46%. Moreover, thickness was shown to be independent of areal mass for the HY-1 sample, while the correlation between the two variables was more evident ($r = 0.63$) for the HY-2 sample. The thickness distributions for both samples were irregular, with HY-1 having a bimodal distribution due to the embossing features, and HY-2 having significant positive skewness unrelated to the melt bonding indentations.

The polymer extruded samples were both formed by similar processes, but the post forming processes of embossing and bonding significantly influenced the structure of PE-2. The stochastic structure of PE-1 had thickness and areal density distributions similar to the wet laid samples. The correlation between the two samples ($r = 0.651$) suggests that this material might be modeled using a bivariate normal distribution, which was not performed in this study. It does suggest that in the absence of calendering or embossing, these materials may be treated as near ideal fibrous systems. The PE-2 sample was heavily embossed and calendered. The embossed and background regions were partitioned using the feature geometry, which clearly distinguished the structural distributions of the two regions. The nature of densification on embossing appeared different than what was observed for the hybrid samples. This was attributed to the thickness of the PE-2 sample and the elastic response of the low density (377 kg m^{-3}) web.

The wet laid samples had structural distributions that were quite similar to paper, as expected based on their composition and forming process. The mass, thickness and

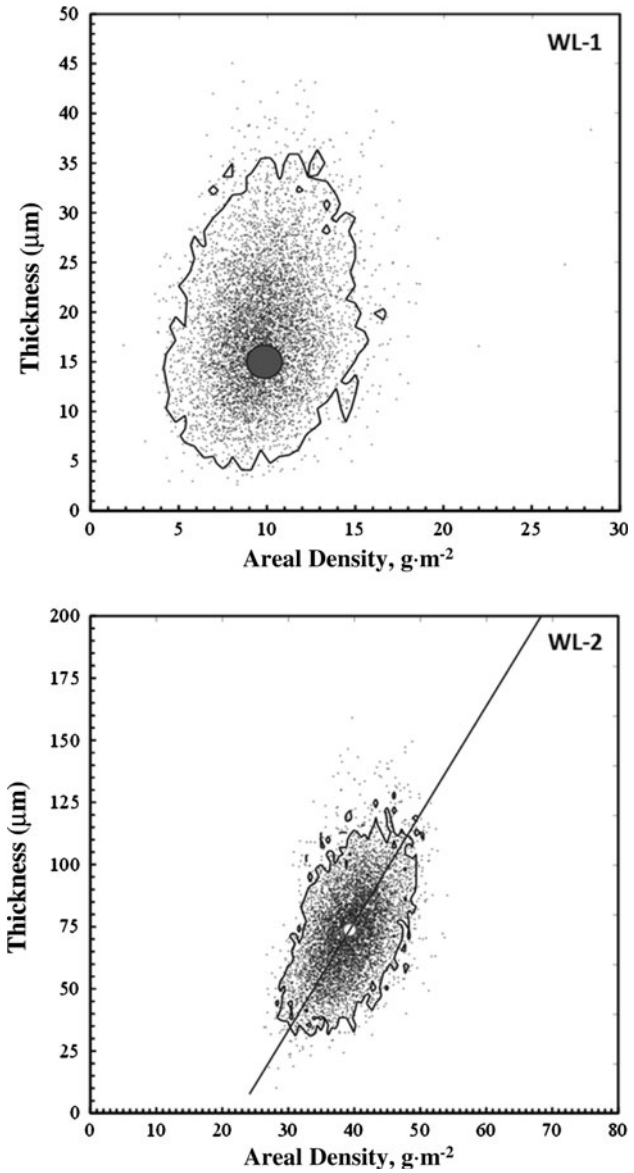

Fig. 20 Distribution of thickness versus grammage for samples WL-1 (*top*) and WL-2 (*bottom*). The background region extends to thicker values and is marked with a *square* at the mean of the distribution. The embossed region is marked with *circles* in the center. *Lines* indicate the RMA least product regressions of the distributions

density distributions were typical form stochastic web structures where local thickness and mass are interdependent. The WL-1 sample had an areal density of 13.1 g m^{-2} which exceeded the lower limit of measurement for radiography and thickness measurements used in this study. Thus, the apparent independence observed between thickness and areal density ($r = 0.20$) must be examined further. The mean volumetric densities, determined from the local thickness and local areal densities of the two wet laid samples were similar, WL-1: 0.591 kg m^{-3} and WL-2: 0.559 kg m^{-3}.

Future work will focus on applying the information obtained from structural mapping and distributions analysis to the material properties that influence performance.

Acknowledgements The authors gratefully acknowledge the financial support of the Research Foundation of the State of New York and the Kimberly-Clark Corporation. The helpful assistance of Dr. Robert Hanna and William Burry of the State University of New York, College of Environmental Science and Forestry is also appreciated.

References

1. Kortschot MT (1997) In: Baker CF (ed) The fundamentals of papermaking materials: transactions of the 11th fundamental research symposium, Cambridge. Pira International, Leatherhead
2. Wagner JR (1993) Tappi J 76(4):190
3. Jeong SH, Kim SH, Hong CJ (2001) Fibers Polym 2(3):164
4. Kallmes A, Scharcanski J, Dodson CTJ (2000) In: Paper presented at the international nonwovens technical conference, Dallas
5. Farnood RR (2009) In: I'Anson SJ (ed) Advances in pulp and paper research: transactions of the 14th fundamental research symposium, Oxford. The Pulp and Paper Fundamental Research Society, Aberystwyth
6. Tydeman PA (1964) Br Pap Board Ind Res Assoc Bull 36(10):10
7. Attwood D, Parker JR (1962) Pap Technol 3(5):435
8. Keller DS, Pawlak JJ (2001) J Pulp Pap Sci 27(4):117
9. Tomimasu H, Luner P, Hanna RB (1989) In: Baker CF (ed) The Fundamentals of Papermaking. Transaction of the 9th Fundamental Research Symposium, Cambridge. Mechanical Engineering Publications Ltd., London
10. Keller DS, Luner P (1998) Rev Sci Instrum 69(6):2495
11. Farrington TE (1988) Tappi J 71(5):140
12. Tomimasu H, Kim D, Suk M, Luner P (1991) Tappi J 74(7):165
13. Sara H (1978) The characterization and measurement of paper formation with standard deviation and power spectrum. PhD thesis, Helsinki University of Technology, Espoo
14. Komppa A (1982) J Phys E Sci Instrum 15(10):1119
15. Cresson TM, Tomimasu H, Luner P (1990) Tappi J 73(7):153
16. Ng WK, Dodson CTJ (1995) In: 1995 International paper physics conference (CPPA and TAPPI): 49–53 (CPPA Technical Section). Eng. Publ. Ltd, London
17. Johnston RF, Pickett SC, Barker DL (1990) Electrophoresis 11(5):355
18. Izumi O, Yoshida Y (1999) In: Development and application of a system for determining paper nonuniformity 66th pulp and paper research conference, Morioka, pp 94–99
19. Sung YJ (2002) PhD thesis, SUNY College of Environmental Science and Forestry
20. Sung YJ, Ham CH, Kwon O, Lee HL, Keller DS (2005) In: I'Anson SJ (ed) Advances in paper science and technology: transactions of the 13th fundamental research symposium, Cambridge. The Pulp and Paper Fundamental Research Society, Peterborough
21. Axelsson M, Svensson S (2010) Pattern Anal Appl 13(2):159
22. Holmstad R, Antoine C, Nygard P, Helle T (2003) Pulp Pap Canada 104(7):47
23. Branca D (2007) Uniformity of low density fibrous structures and the effects of manufacturing processes on apparent density. MS thesis, SUNY College of ESF, Syracuse
24. Keller DS, Branca D, Kwon O (2009) In: I'Anson SJ (ed) Advances in pulp and paper research. Transactions of 14th

fundamental research symposium. Fundamental Research Society, Oxford
25. Dodson CTJ, Oba Y, Sampson WW (2001) Appita J 54(4):385
26. Dodson CTJ, Oba Y, Sampson WW (2001) J Stat Phys 102 (1–2):345
27. Sung YJ, Keller DS (2008) Appita J 61(1):28
28. Vaughn EA (2005) Nonwoven fabrics: sampler and technology reference. INDA Association of the Nonwoven Fabrics Industry, Cary
29. TAPPI Standard Test Methods T410 om-97 (1998) In: Grammage of paper and paperboard (weight per unit area). TAPPI Press, Atlanta
30. TAPPI Standard Test Methods T411 om-97 (1998) In: Thickness (Caliper) of paper, paperboard, and combined board. TAPPI PRESS, Atlanta
31. Kimura M, Matsui S, Kadoya T (1984) Jpn Tappi 38(12):1227
32. Kimura M, Matsui S, Nakato K (1985) J Soc Fiber Sci Technol Jpn (Sen-i Gakkaishi) 41(7):T308
33. Schultz-Eklund O, Fellers C, Johansson P (1992) Nordic Pulp Pap Res J 7(3):133–139
34. TAPPI T402 sp-03 (2003) Standard conditioning, testing atmosphere for paper, board, pulp handsheets, related products. TAPPI Press, Atlanta
35. Kwon O, Hanna R (2010) Strain 46(6):566
36. Deng M, Dodson CTJ (1994) Paper: an engineered stochastic structure. TAPPI Press, Atlanta
37. Sampson WW (2009) Modelling stochastic fibrous materials with mathematica. Engineering materials and processes. Springer-Verlag, London
38. Draper N, Smith H (1998) Applied regression analysis (Wiley series in probability and statistics). Wiley-Interscience, New York